Hindawi
International Journal of Aerospace Engineering
Volume 2022, Article ID 7695535, 14 pages
https://doi.org/10.1155/2022/7695535

Research Article

Adaptive Robust Control and Active Vibration Suppression of Dumbbell-Shaped Spacecraft

Q. M. Ai,[1] **T. Liu**,[1] **H. W. Fan**,[2] **J. M. Chen**,[3] **and S. L. Li**[1]

[1]*School of Astronautics, Harbin Institute of Technology, Harbin, Heilongjiang 150001, China*
[2]*School of Mechatronics Engineering, Harbin Institute of Technology, Harbin, Heilongjiang 150001, China*
[3]*Harbin Federation of Trade Unions, Harbin, Heilongjiang 150026, China*

Correspondence should be addressed to S. L. Li; lishunli@hit.edu.cn

Received 1 July 2022; Revised 22 July 2022; Accepted 4 August 2022; Published 8 September 2022

Academic Editor: Erkan Kayacan

In this paper, the dynamic modelling of a new configuration spacecraft is investigated. The significance of dumbbell-shaped spacecraft to deep space exploration and the configuration of dumbbell-shaped spacecraft are introduced firstly. Then, the vibration problem of the dumbbell-shaped spacecraft of large-angle attitude maneuver is investigated, and a control program based on the combination of adaptive robust control (ARC) and component synthesis vibration suppression method-seven-section path planning (CSVS-SPP) is proposed. The large-angle attitude maneuver route of the spacecraft, which serves as the reference path, is planned using the CSVS-SPP approach, and the attitude controller is designed using the ARC. This program can effectively reduce the influence of external disturbance and parameter uncertainty on the system performance while completing attitude maneuver and suppress the vibration of the flexible beam during large-angle attitude maneuver. The numerical simulations show the superiority and effectiveness of the proposed ARC+CSVS-SPP.

1. Introduction

With the rapid development of space technology and space science, deep space exploration is playing an increasingly important role in space activities. The nuclear-powered spacecraft has become an important choice for deep space exploration because the spacecraft needs to work for a long time and consumes a lot of energy [1]. Because the heat and radiation generated by the nuclear reactor can damage electronic equipment and other facilities on the spacecraft, it is necessary to separate the nuclear reactor and the main body of the spacecraft when designing the nuclear-powered spacecraft. Traditional spacecraft is mainly composed of central rigid body and deployable flexible appendages, such as solar panels [2, 3], synthetic aperture radar (SAR) [4], and communication antenna [5]. The dumbbell-shaped spacecraft is rigid at both ends and connected by a large flexible truss in the middle. The structure and mass distribution are quite different from those of traditional spacecraft [6]. Therefore, its dynamic characteristics, attitude control, and vibration suppression will be different.

More and more attention has been paid to the dynamics of dumbbell-shaped spacecraft, and a lot of research has been done. Abouelmagd et al. [7] showed that when the influence of the zonal harmonic parameter is not zero, the pass trajectory of the dumbbell-shaped spacecraft is periodic. Then, they further studied the equilibrium points' position and the stability of the trajectory [8]. Liang and Liao [9] proved that the vibration of dumbbell-shaped spacecraft has at least two periodic solutions; in these two periodic solutions, at least one periodic solution is unstable. Those researches above mainly focus on equilibrium and stability analysis, and the mass and flexibility of the flexible beams are not considered in the dynamic model, which cannot meet the requirements of dynamic simulation and controller design.

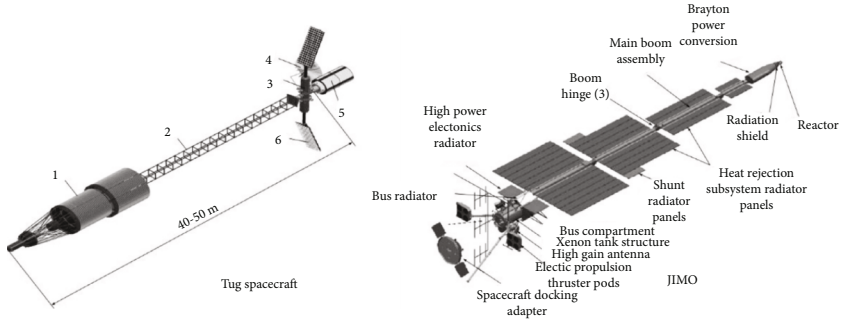

Figure 1: Existing dumbbell-shaped spacecraft design.

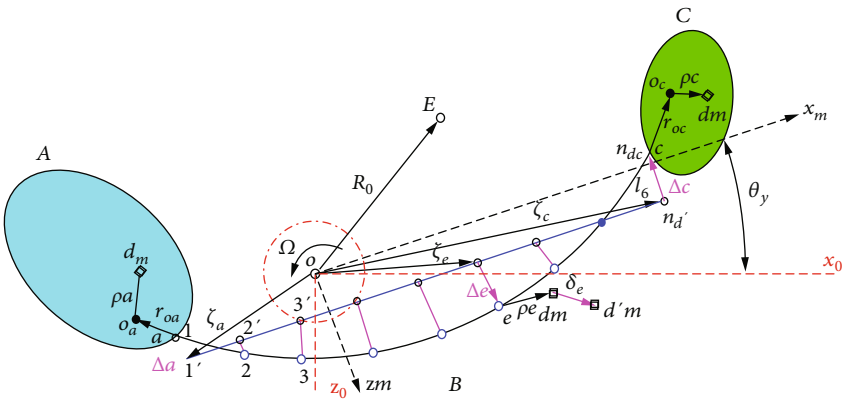

Figure 2: Vector description and coordinate system definition.

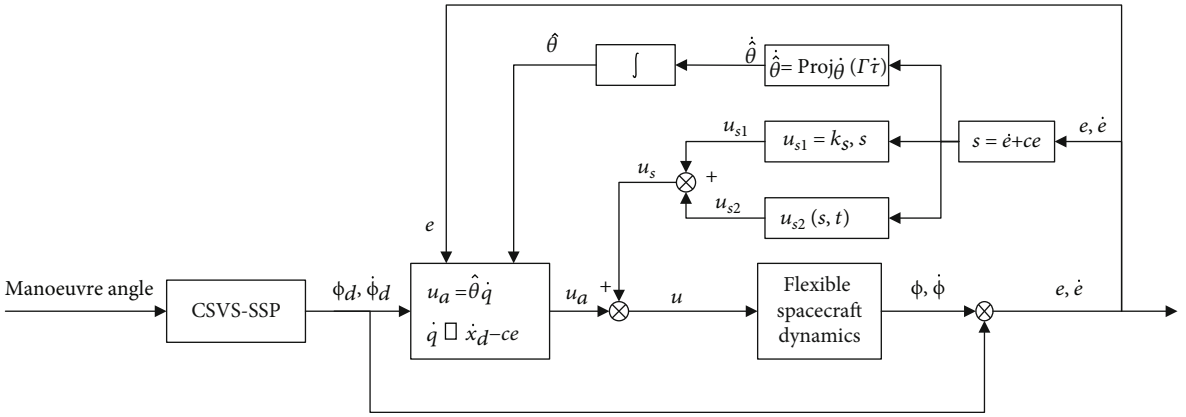

Figure 3: Robust adaptive attitude controller for dumbbell-shaped spacecraft.

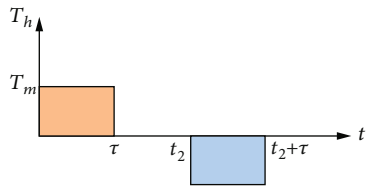

Figure 4: Bang-off-bang maneuver command.

During the past decades, a large amount of efforts have been put into designing control systems for attitude maneuver control of flexible spacecraft, such as trajectory tracking control [10], variable structure control [11, 12], active disturbance rejection control [13], fault-tolerant control [14], and L1 adaptive control (AC) [15]. Recently, Sun et al. and Qinqin et al. have proposed a new control theory called adaptive robust control (ARC), which is used for various systems with both parameter uncertainty and uncertain nonlinearity [16, 17]. By employing online parameter adaptation to reduce the effects of parameter uncertainty and

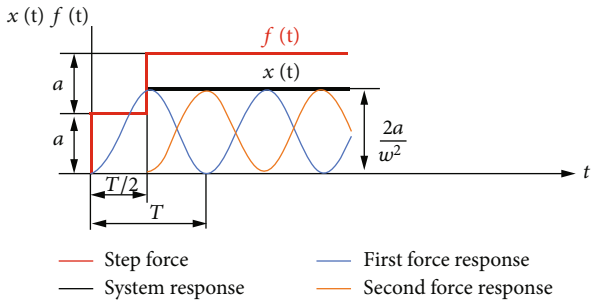

Figure 5: Effect of two equal amplitude step forces on vibration system.

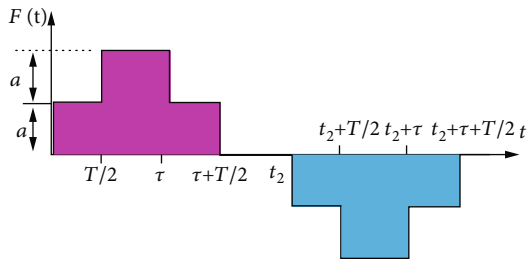

Figure 6: CSVS-SPP torque diagram.

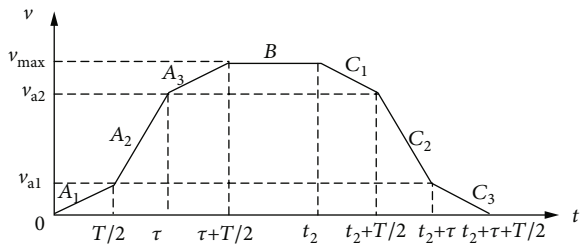

Figure 7: Sketch of CSVS-SPP maneuver path.

robust control law to control the influence of various uncertainties, ARC can maintain the theoretical performance results of AC and DRC [18]. In order to solve the conflict between the two design methods, the projection parameter adaptive control law is used [19]. Since ARC has the advantages of high final tracking accuracy and guaranteed transient performance, it is of great significance to study the applicability of ARC theory in attitude maneuver control of dumbbell-shaped spacecraft.

Rapid maneuver of flexible spacecraft with large-angle attitude is a necessary condition to meet the requirements of specific missions. During and after manipulation, flexible accessories usually deform elastically. Path planning technology has been widely used in spacecraft control [23]. The angular acceleration and velocity of spacecraft during attitude maneuver are limited due to the limitation of the function of attitude actuator and the capability of the measuring device. Therefore, it is necessary to design an attitude maneuver path in order to plan an appropriate angular position, which would not easily arouse the vibration of flexible appendages. Up to now, many attitude path planning methods have been proposed, such as bang-coast-bang (BCB) path planning [24], smooth bang-bang contour [25], S contour [26], and parabolic contour [27]. These methods have not been applied to the path planning of dumbbell-shaped spacecraft with large-angle attitude maneuver.

In the dynamic modeling of dumbbell-shaped spacecraft, the spacecraft is generally simplified as a massless rigid or flexible rod connecting two particles or cabins without considering the moment of inertia of cabins at both ends. In the process of large-angle attitude maneuver, the accuracy and efficiency of attitude maneuver are not considered. It cannot meet the requirements of dynamic simulation and controller design.

Obviously, the existing dumbbell-shaped spacecraft dynamics model cannot meet the requirements of attitude control and vibration suppression with large angle, high precision, and high stability. As shown in Figure 1, the spacecraft is mainly composed of nuclear reactor, large flexible beam, and active end. This is a typical rigid-flexible coupling multibody system. It is necessary to establish an accurate dynamic model of dumbbell-shaped spacecraft. In addition, the model is simplified reasonably, which is convenient for controller design. It is necessary to further study the large-angle attitude control and attitude path planning, so as to meet the accuracy requirements and minimize the vibration of flexible appendages.

The objective of this paper is to build a dumbbell-shaped spacecraft dynamics model to complete high-angle attitude maneuver.

The main contributions are as follows: first, a dynamic model of the dumbbell-shaped spacecraft has been established using the Newton-Euler technique and Lagrange equations in accordance with the multibody dynamics principle. Second, a seven-segment trajectory planning approach based on the component force synthesis method is provided to give a reference trajectory for the large-angle attitude maneuver of the dumbbell configuration spacecraft. Third, a control approach based on the fusion of the adaptive robust control (ARC) technique and component force synthesis seven-segment attitude path planning method (CSVS-SPP) is presented to address the vibration issue of the flexure beam when the dumbbell-shaped spacecraft executes large-angle attitude maneuvers.

The remainder of this paper is organized as follows: the next section focuses on taking the dumbbell-shaped spacecraft in the unfolded state as the research object; the dynamic modeling of rigid-flexible coupling dumbbell-shaped spacecraft is carried out by the Newton-Euler and Lagrange method. In the third part, aiming at the attitude control problem of spacecraft with external disturbances and parameter uncertainties, a control law based on the idea of adaptive robust control is proposed, and strict stability proof is provided. In the fourth part, a seven-section path planning method based on component synthesis active vibration suppression is proposed, which is combined with ARC to realize attitude control and vibration suppression. The fifth part is a numerical simulation analysis. The sixth part is the conclusion.

Table 1: Parameters of dumbbell-shaped spacecraft.

Component	Items (unit)	Parameter
Main body	Mass (kg)	7000
	Length × width × height (m)	6 × 3 × 3
	Moment of inertia	Diag (6000,13000,13000)
Flexible beam	Mass (kg)	1600
	Length × outer diameter × inner diameter	30 × 0.06 × 0.055
	Moment of inertia	Diag (150,1.2e5,1.2e5)
Nuclear reactor	Mass (kg)	3000
	Length × width × height (m)	2 × 2 × 2
	Moment of inertia	Diag (900,8000,8000)

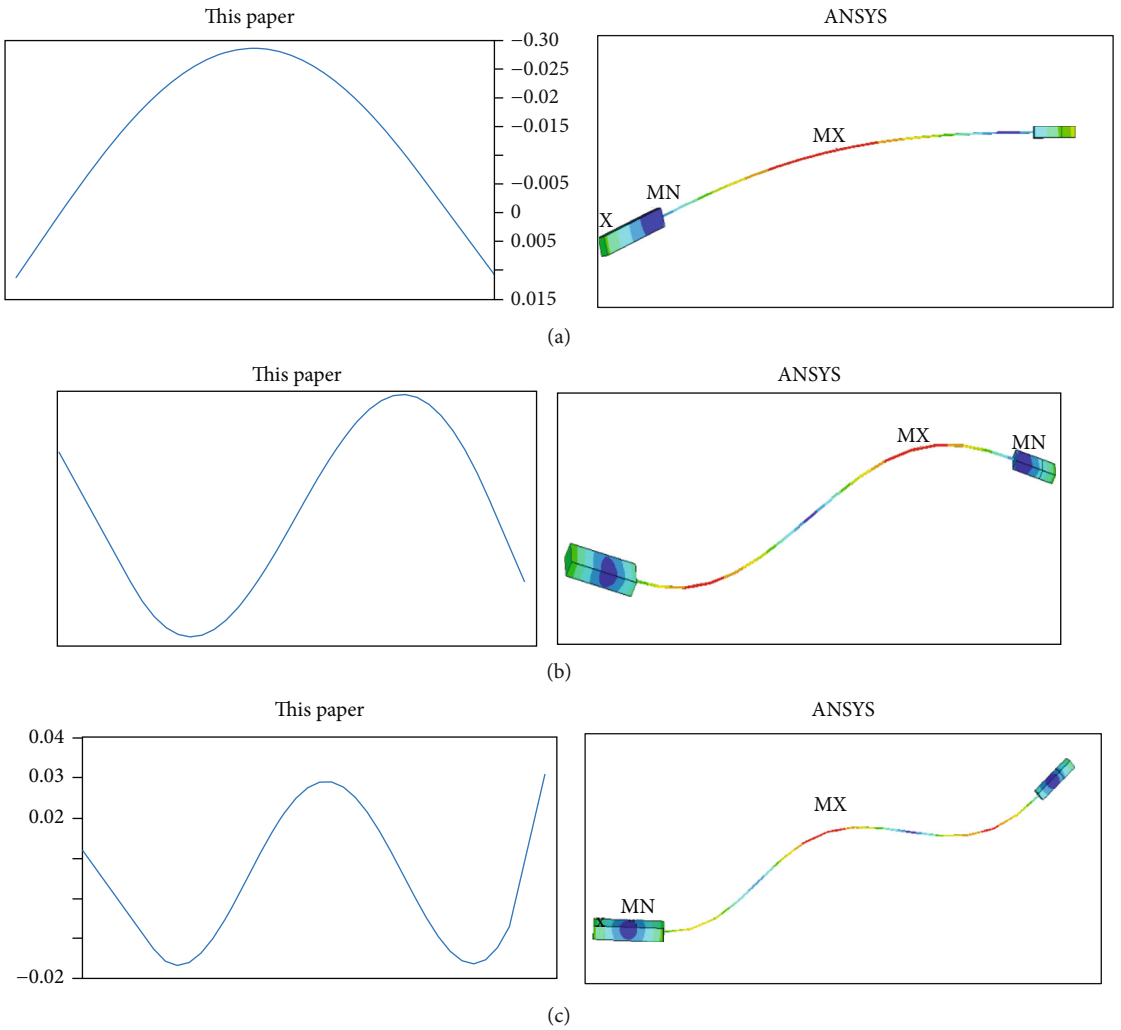

Figure 8: Modal shape of dumbbell-shaped spacecraft.

2. Dynamic Model of Dumbbell-Shaped Spacecraft

As shown in Figure 2, the simplified model of the system is mainly composed of the equivalent flexible beam in the deployed state, the active end, and the nuclear reactor. The active end and nuclear reactor are assumed to be rigid bodies. $\boldsymbol{e}^E$is defined as inertial coordinate system, $\boldsymbol{e}^0$ is orbital coordinate system, $\boldsymbol{e}^m$ is fixed coordinate system, $\boldsymbol{e}^a$is active end coordinate system, $\boldsymbol{e}^c$is nuclear reactor coordinate

Table 2: Natural frequency comparison.

Modal	This paper (Hz)	ANSYS (Hz)
First modal (bending mode)	0.2230	0.2234
Second modal (bending mode)	0.6971	0.7054
Third modal (bending mode)	1.3431	1.3803

Table 3: CSVS-SPP planning parameters.

No.	Start time (s)	End time (s)	Control torque (N·m)
Section 1	0	$T_1/2$	$T_y/2$
Section 2	$T_1/2$	τ	T_y
Section 3	τ	$\tau + T_1/2$	$T_y/2$
Section 4	$\tau + T_1/2$	t_2	0
Section 5	t_2	$t_2 + T_1/2$	$-T_y/2$
Section 6	$t_2 + T_1/2$	$t_2 + \tau$	$-T_y$
Section 7	$t_2 + \tau$	$t_2 + \tau + T_1/2$	$-T_y/2$

system, and $\boldsymbol{e}^e$ is unit coordinate system. o, o_a, and o_c are the centroids of systems $A$and C, respectively; $R_0$is the vector from the inertial reference point to the center of mass of the system; $\boldsymbol{\zeta}_a$ and $\boldsymbol{\zeta}_c$ are the vectors from the center of mass of the system to the active end and the connection point between the nuclear reactor and the flexible beam.

As shown in Figure 2, the position vectors of any particle dm on the active end, flexible beam, and nuclear reactor are as follows:

$$\begin{aligned} \boldsymbol{s}_a &= \boldsymbol{R}_0 + \boldsymbol{\zeta}_a + \boldsymbol{\Delta}_a + \boldsymbol{r}_{o_a} + \boldsymbol{\rho}_a, \\ \boldsymbol{s}_c &= \boldsymbol{R}_0 + \boldsymbol{\zeta}_c + \boldsymbol{\Delta}_c + \boldsymbol{r}_{o_c} + \boldsymbol{\rho}_c, \\ \boldsymbol{s}_b^e &= \boldsymbol{R}_0 + \boldsymbol{\zeta}_a + \sum_{k=1}^{e-1} \boldsymbol{l}_k + \boldsymbol{\rho}_e + \boldsymbol{\delta}^e, \quad e = 1, 2, \cdots, n_e. \end{aligned} \tag{1}$$

Velocity is the time derivative of position, and the velocity vector is divided into two parts: those related to elastic deformation and those independent of elastic deformation:

$$\begin{aligned} \boldsymbol{v}_a &= \dot{\boldsymbol{s}}_a = \underbrace{\boldsymbol{v}_0 + \boldsymbol{\Omega} \times \left(\boldsymbol{\zeta}_a + \boldsymbol{r}_{o_a} + \boldsymbol{\rho}_a\right)}_{\boldsymbol{v}_{\Gamma a}} + \overset{\oplus}{\boldsymbol{\Delta}}_a + \boldsymbol{\Omega} \times \boldsymbol{\Delta}_a, \\ \boldsymbol{v}_c &= \dot{\boldsymbol{s}}_c = \underbrace{\boldsymbol{v}_0 + \boldsymbol{\Omega} \times \left(\boldsymbol{\zeta}_c + \dot{\boldsymbol{r}}_{o_c} + \dot{\boldsymbol{\rho}}_c\right)}_{\boldsymbol{v}_{\Gamma c}} + \overset{\oplus}{\boldsymbol{\Delta}}_c + \boldsymbol{\Omega} \times \boldsymbol{\Delta}_c, \\ \boldsymbol{v}_e &= \dot{\boldsymbol{s}}_b^e = \underbrace{\boldsymbol{v}_0 + \boldsymbol{\Omega} \times \left(\boldsymbol{\zeta}_1 + \sum_{k=1}^{e-1} \boldsymbol{l}_k + \boldsymbol{\rho}_e\right)}_{\boldsymbol{v}_{\Gamma e}} + \boldsymbol{\Omega} \times (\boldsymbol{\Delta}_1 + \boldsymbol{\delta}^e) + \overset{\oplus}{\boldsymbol{\Delta}}_1 + \overset{\oplus}{\boldsymbol{\delta}}^e, \end{aligned} \tag{2}$$

where$\boldsymbol{\Omega}$ is the rotation vector of the system around the center of mass and $x^{\oplus}$ is the relative derivative of the vector. The velocity is transformed into the form expressed in generalized coordinates as follows:

$$\begin{aligned} \boldsymbol{v}_a &= \boldsymbol{v}_{\Gamma a} + \underline{\boldsymbol{e}}_m^T \underline{\beta}_1^1 \dot{\underline{d}} + \underline{\boldsymbol{e}}_m^T \underline{\Omega}^{\times} \underline{\beta}_1^1 \underline{d}, \\ \boldsymbol{v}_c &= \boldsymbol{v}_{\Gamma c} + \underline{\boldsymbol{e}}_m^T \underline{\beta}_3^{n_e} \dot{\underline{d}} + \underline{\boldsymbol{e}}_m^T \underline{\Omega}^{\times} \underline{\beta}_3^{n_e} \underline{d}, \\ \boldsymbol{v}_e &= \boldsymbol{v}_{\Gamma e} + \underline{\boldsymbol{e}}_m^T \left(\underline{N}^e \underline{P}^e + \underline{\beta}_1^1\right) \dot{\underline{d}} + \underline{\boldsymbol{e}}_m^T \underline{\Omega}^{\times} \left(\underline{N}^e \underline{P}^e + \underline{\beta}_1^1\right) \underline{d}, \end{aligned} \tag{3}$$

where $\underline{\beta}_x^y$ represents a sparse matrix of $3 \times n$ dimensions, x is the position of the line displacement or angular displacement in the matrix, and y represents the unit. $\underline{\Omega}^{\times}$ is the cross product operator of $\underline{\Omega}$. d represents the vibration of the whole body, $\underline{N}^e$ is shape function, $\underline{P}^e$ represents the contact matrix, and $\dot{\underline{d}}$is the derivative.

Acceleration is the derivative of velocity, so the acceleration of any particle of each body is as follows:

$$\begin{aligned} \boldsymbol{a}_a &= \dot{\boldsymbol{v}}_a = \boldsymbol{a}_0 + \dot{\boldsymbol{\Omega}} \times \left(\boldsymbol{\zeta}_a + \boldsymbol{r}_{o_a} + \boldsymbol{\rho}_a\right) + \overset{\oplus\oplus}{\boldsymbol{\Delta}}_a + \boldsymbol{\varphi}_{aa}, \\ \boldsymbol{a}_c &= \dot{\boldsymbol{v}}_c = \boldsymbol{a}_0 + \dot{\boldsymbol{\Omega}} \times \left(\boldsymbol{\zeta}_c + \boldsymbol{r}_{o_c} + \boldsymbol{\rho}_c\right) + \overset{\oplus\oplus}{\boldsymbol{\Delta}}_c + \boldsymbol{\varphi}_{ac}, \\ \boldsymbol{a}_e &= \dot{\boldsymbol{v}}_e = \boldsymbol{a}_0 + \dot{\boldsymbol{\Omega}} \times \left(\boldsymbol{\zeta}_1 + \sum_{k=1}^{e-1} \boldsymbol{l}_k + \boldsymbol{\rho}_e\right) + \overset{\oplus\oplus}{\boldsymbol{\Delta}}_1 + \overset{\oplus\oplus}{\boldsymbol{\delta}}^e + \boldsymbol{\varphi}_{ae}, \quad e = 1, 2, \cdots, n_e, \end{aligned} \tag{4}$$

where $x^{\oplus\oplus}$ represents the relative acceleration and $\boldsymbol{\varphi}_{ax}$ is the nonlinear term of each body.

$$\begin{aligned} \boldsymbol{\varphi}_{aa} &= \dot{\boldsymbol{\Omega}} \times \boldsymbol{\Delta}_a + \boldsymbol{\Omega} \times \left[\boldsymbol{\Omega} \times \left(\boldsymbol{\zeta}_a + \boldsymbol{\Delta}_a + \boldsymbol{r}_{o_a} + \boldsymbol{\rho}_a\right)\right] + 2\boldsymbol{\Omega} \times \overset{\oplus}{\boldsymbol{\Delta}}_a, \\ \boldsymbol{\varphi}_{ac} &= \dot{\boldsymbol{\Omega}} \times \boldsymbol{\Delta}_c + \boldsymbol{\Omega} \times \left[\boldsymbol{\Omega} \times \left(\boldsymbol{\zeta}_c + \boldsymbol{\Delta}_c + \boldsymbol{r}_{o_c} + \boldsymbol{\rho}_c\right)\right] + 2\boldsymbol{\Omega} \times \overset{\oplus}{\boldsymbol{\Delta}}_c, \\ \boldsymbol{\varphi}_{ae} &= 2\underline{\Omega}^{\times} \underline{N}^e \underline{P}^e \dot{\underline{d}}. \end{aligned} \tag{5}$$

The acceleration term is divided into generalized displacement-related and unrelated forms, which are expressed as follows:

$$\begin{aligned} \boldsymbol{a}_a &= \boldsymbol{a}_{\Gamma a} + \underline{\boldsymbol{e}}_m^T \underline{\beta}_1^1 \ddot{\underline{d}} + \boldsymbol{\varphi}_{aa}, \\ \boldsymbol{a}_c &= \boldsymbol{a}_{\Gamma c} + \underline{\boldsymbol{e}}_m^T \underline{\beta}_3^{n_e} \ddot{\underline{d}} + \boldsymbol{\varphi}_{ac}, \\ \boldsymbol{a}_e &= \boldsymbol{a}_{\Gamma e} + \underline{\boldsymbol{e}}_m^T \left(\underline{N}^e \underline{P}^e + \underline{\beta}_1^1\right) \ddot{\underline{d}} + \boldsymbol{\varphi}_{ae}. \end{aligned} \tag{6}$$

The attitude motion equation is the equilibrium between the inertial moment and the external moment relative to the

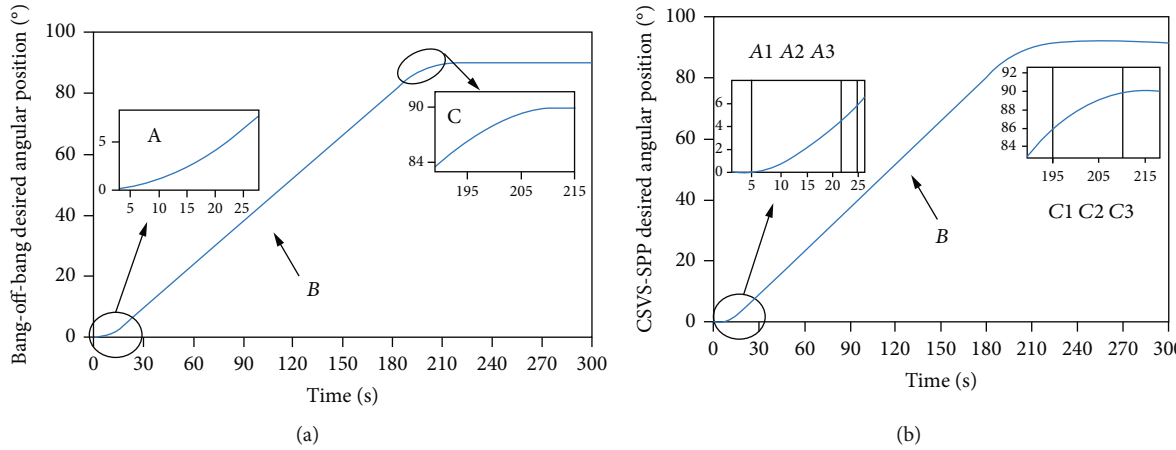

(a) (b)

Figure 9: Desired attitude angular position: (a) bang-off-bang desired angular position and (b) CSVS-SPP desired angular position.

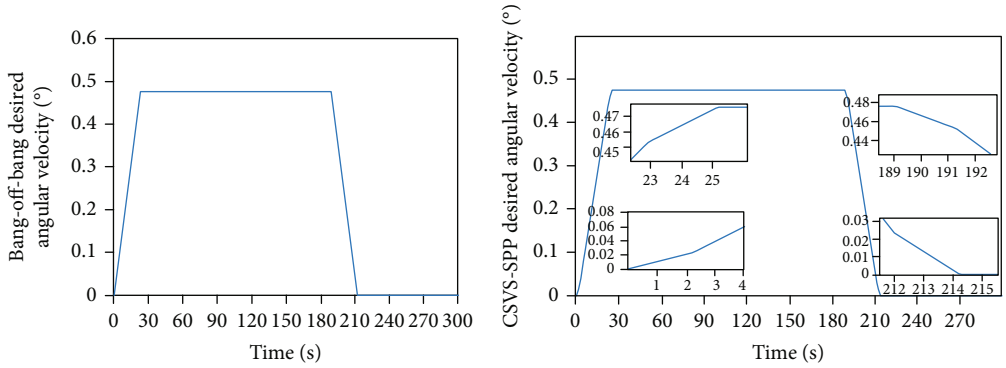

(a) (b)

Figure 10: Desired angular velocity: (a) bang-off-bang desired angular velocity and (b) CSVS-SPP desired angular velocity.

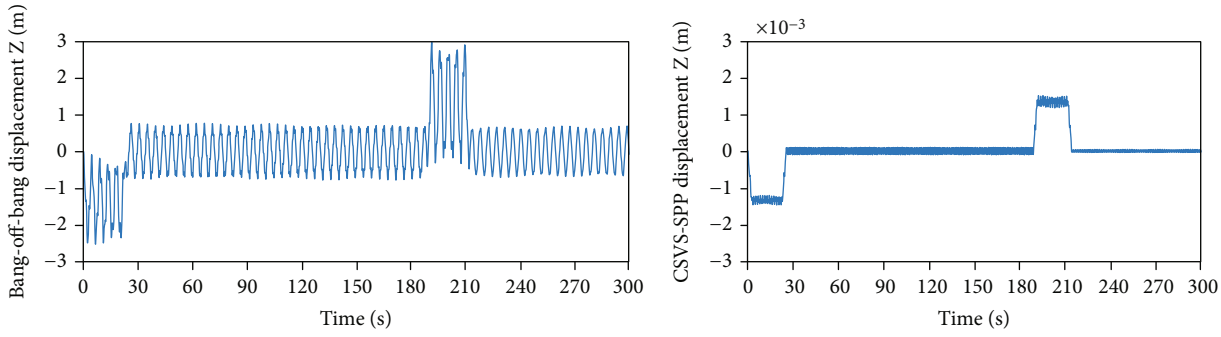

(a) (b)

Figure 11: Vibration response: (a) bang-off-bang attitude maneuver time and vibration amplitude and (b) CSVS-SPP attitude maneuver time and vibration amplitude.

center of mass of the system, and the equation is as follows:

$$\int_A (\boldsymbol{\zeta}_a + \boldsymbol{\Delta}_a + \boldsymbol{r}_{o_a} + \boldsymbol{\rho}_a) \times \boldsymbol{a}_a \mathrm{d}m + \int_C (\boldsymbol{\zeta}_c + \boldsymbol{\Delta}_c + \boldsymbol{r}_{o_c} + \boldsymbol{\rho}_c) \times \boldsymbol{a}_c \mathrm{d}m, + \sum_{e=1}^{n_e} \int_e \left(\boldsymbol{\zeta}_1 + \sum_{i=1}^{e-1} \boldsymbol{l}_i + \boldsymbol{\rho}_e + \boldsymbol{\delta}^e \right) \times \boldsymbol{a}_e \mathrm{d}m = \underline{u}. \tag{7}$$

The acceleration term of Equation (6) is brought into Equation (7), and the second-order small quantity in the calculation process is omitted by using the centroid relationship of the system, and the following results are obtained:

$$\underline{J}_{\Sigma}^{(o)} \ddot{\underline{\phi}} + \underline{H}_{\Sigma} \ddot{\underline{d}} = \underline{u} + \underline{\boldsymbol{\varphi}}_{ati} - \underline{\Omega}^{\times} \underline{J}_{\Sigma}^{(o)} \cdot \underline{\Omega}, \tag{8}$$

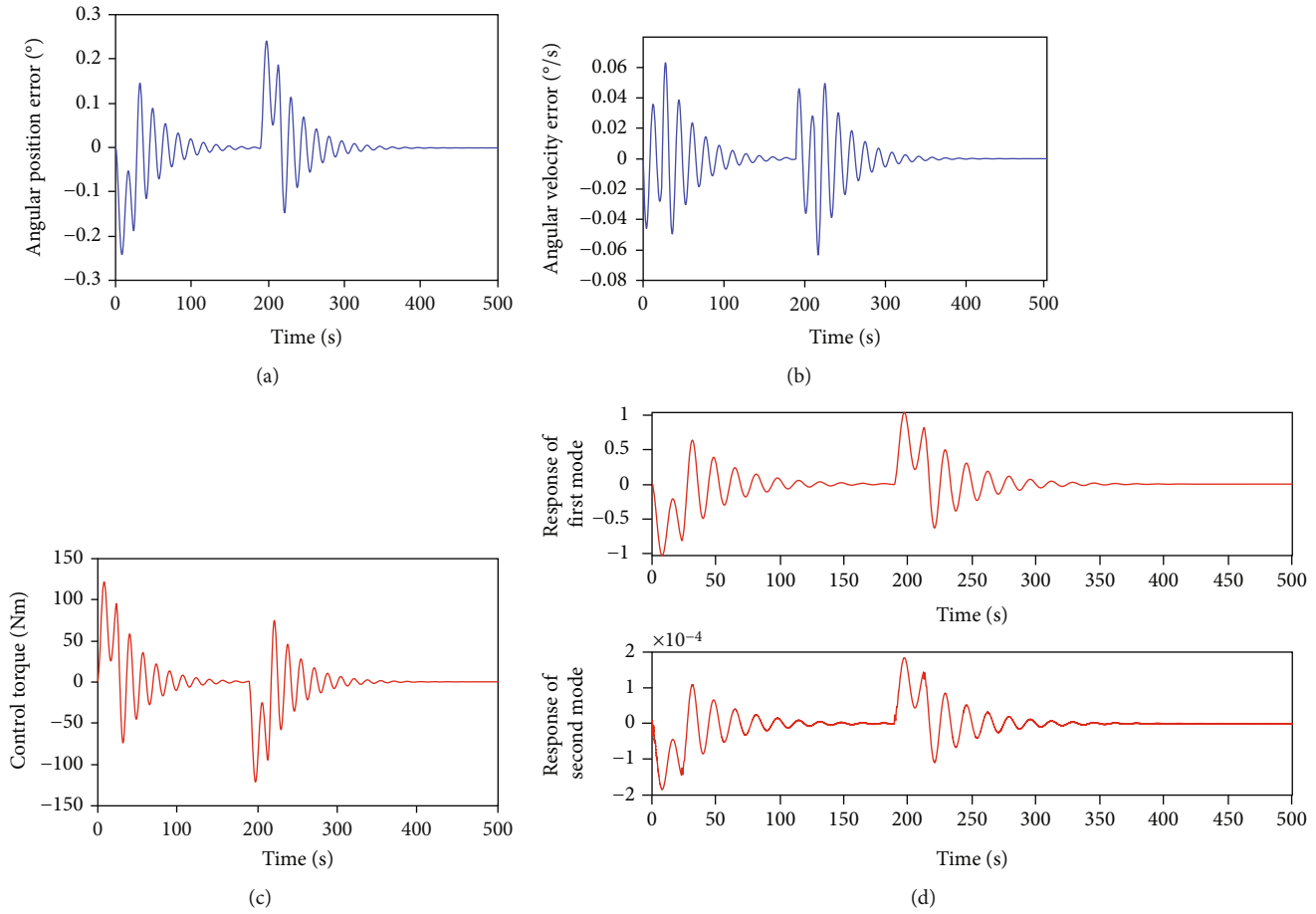

FIGURE 12: Simulation results of PD control (a) angular position error of PD control, (b) angular velocity error of PD control, (c) control torque profile of PD control, and (d) response of the first two modes.

where $\underline{J}_{\Sigma}^{(o)}$ represents the moment of inertia of the system relative to the center of mass, and the dimension is 3×3, and $\underline{H}_{\Sigma}$ is the cross-influence matrix. The nonlinear term is as follows:

$$\underline{\boldsymbol{\varphi}}_{ati} = \sum_{e=1}^{n_e} \int_e \left(\underline{\zeta}_1^{\times} + \sum_{k=1}^{e-1} \underline{l}_k^{\times} + \underline{\rho}_e^{\times} \right) \underline{\varphi}_b^e \mathrm{dm} + \int_C \left(\underline{\zeta}_{n_d}^{\times} + \underline{r}_{o_c}^{\times} + \underline{\rho}_c^{\times} \right) \underline{\varphi}_a \mathrm{dm} + \int_A \left(\underline{\zeta}_1^{\times} + \underline{r}_{o_a}^{\times} + \underline{\rho}_a^{\times} \right) \underline{\varphi}_c \mathrm{dm}. \tag{9}$$

The Lagrange equation of the second kind is used to derive the system vibration equation as follows:

$$\frac{d}{\mathrm{dt}} \left(\frac{\partial E}{\partial \underline{d}} \right) - \left(\frac{\partial E}{\partial \underline{d}} \right) = \underline{Q}, \tag{10}$$

where $\underline{Q}$ is generalized force and $\underline{d}$ is generalized displacement, that is, the displacement of each node of the beam, and the displacement of each node is 6 dimensions.

$$\underline{d} = \begin{bmatrix} \underline{d}_1 \\ \underline{d}_2 \\ \vdots \\ \underline{d}_{6n_d} \end{bmatrix}, \tag{11}$$

where n_d is the number of nodes and E is the kinetic energy of the system (the potential energy is implied in the generalized force $\underline{Q}$). $\underline{d}$ and $\underline{Q}$ are the vectors of the same dimension, and $\underline{Q}$ includes the elastic restoring force, damping force, and external force. The kinetic energy of dumbbell-shaped spacecraft system is expressed as follows:

$$\begin{aligned} E &= E_a + E_c + \sum_{e=1}^{n_e} E_e, \\ E_a &= \frac{1}{2} \int_A \boldsymbol{v}_a \cdot \boldsymbol{v}_a \mathrm{dm}, \\ E_c &= \frac{1}{2} \int_C \boldsymbol{v}_c \cdot \boldsymbol{v}_c \mathrm{dm}, \\ E_e &= \frac{1}{2} \int_e \boldsymbol{v}_e \cdot \boldsymbol{v}_e \mathrm{dm}, \end{aligned} \tag{12}$$

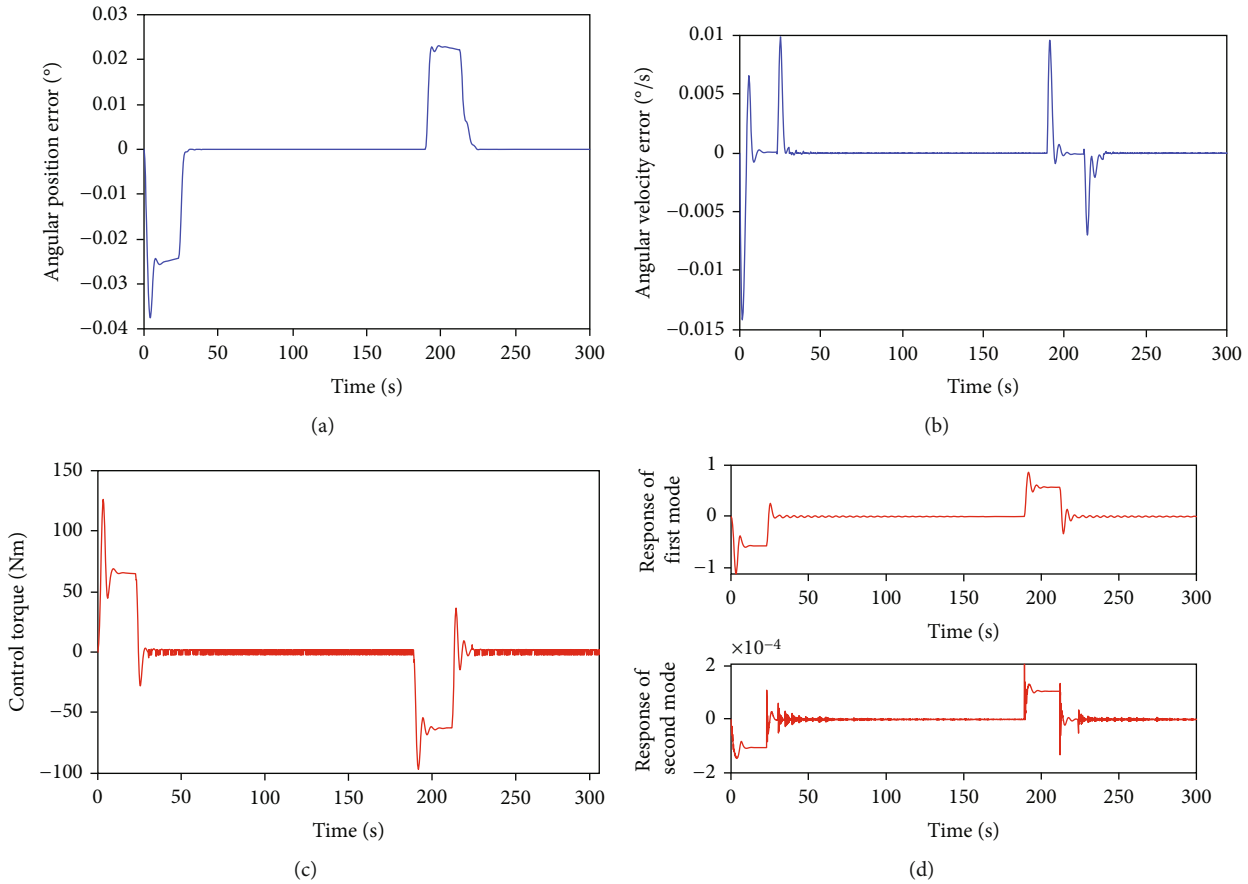

FIGURE 13: Simulation results of DRC control: (a) angular position error of DRC control, (b) angular velocity error of DRC control, (c) control torque profile of DRC control, and (d) response of the first two modes.

where E_a, E_c, and E_e are the kinetic energy of A, C and e unit, respectively, brought into Equation (10) as follows:

$$\int_A \left[\frac{d}{\mathrm{d}t}\left(\frac{\partial \boldsymbol{v}_a}{\partial \underline{\dot{d}}}\cdot \boldsymbol{v}_a\right) - \frac{\partial \boldsymbol{v}_a}{\partial \underline{d}}\cdot \boldsymbol{v}_a\right]\mathrm{d}m + \int_C \left[\frac{d}{\mathrm{d}t}\left(\frac{\partial \boldsymbol{v}_c}{\partial \underline{\dot{d}}}\cdot \boldsymbol{v}_c\right) - \frac{\partial \boldsymbol{v}_c}{\partial \underline{d}}\cdot \boldsymbol{v}_c\right]\mathrm{d}m + \sum_{e=1}^{n_e}\int_e \left[\frac{d}{\mathrm{d}t}\left(\frac{\partial \boldsymbol{v}_e}{\partial \underline{\dot{d}}}\cdot \boldsymbol{v}_e\right) - \frac{\partial \boldsymbol{v}_e}{\partial \underline{d}}\cdot \boldsymbol{v}_e\right]\mathrm{d}m = \underline{Q}_{(n\times 1)}. \tag{13}$$

Equation (2) is brought into Equation (13), and $\underline{Q} = \underline{F} - \underline{h}\,\underline{\dot{d}} - \underline{K}\underline{d}$; Equation (13) is arranged to get

$$\underline{H}_\Sigma^T\underline{\ddot{\phi}} + \underline{M}_\Sigma\underline{\ddot{d}} + \underline{h}_\Sigma\underline{\dot{d}} + \underline{K}\underline{d} = \underline{F} + \underline{\varphi}_{vib}, \tag{14}$$

where $\underline{M}_\Sigma$ is the mass matrix of system, $\underline{h}_\Sigma$ is the damping matrix of system, $\underline{h}_\Sigma\underline{\dot{d}}$ is the damping force of system, $\underline{K}$ is the system stiffness matrix, $\underline{K}\underline{d}$ is the system elastic restoring force, $\underline{F}$ is the external force, and $\underline{\varphi}_{vib}$ is the nonlinear term.

$$\underline{\varphi}_{vib} = \int_A \underline{\beta}_1^{1T}\underline{\varphi}_{aa}\mathrm{d}m + \int_C \underline{\beta}_3^{n_eT}\underline{\varphi}_{ac}\mathrm{d}m + \sum_{e=1}^{n_e}\int_e \underline{P}^{eT}\underline{N}^{eT}\underline{\varphi}_{a_e}\mathrm{d}m. \tag{15}$$

Combining attitude equation (8) and vibration equation (14)

$$\begin{aligned} \underline{J}_\Sigma^{(o)}\underline{\ddot{\phi}} + \underline{H}_\Sigma\underline{\ddot{d}} &= \underline{u} + \underline{\varphi}_{ati}, \\ \underline{H}_\Sigma^T\underline{\ddot{\phi}} + \underline{M}_\Sigma\underline{\ddot{d}} + \underline{h}_\Sigma\underline{\dot{d}} + \underline{K}\underline{d} &= \underline{F} + \underline{\varphi}_{vib}, \end{aligned} \tag{16}$$

write in matrix form

$$\begin{bmatrix} \underline{J}_\Sigma^{(o)} & \underline{H}_\Sigma \\ \underline{H}_\Sigma^T & \underline{M}_\Sigma \end{bmatrix}\begin{bmatrix} \underline{\ddot{\phi}} \\ \underline{\ddot{d}} \end{bmatrix} + \begin{bmatrix} \underline{0} & \underline{0} \\ \underline{0} & \underline{h}_\Sigma \end{bmatrix}\begin{bmatrix} \underline{\dot{\phi}} \\ \underline{\dot{d}} \end{bmatrix} + \begin{bmatrix} \underline{0} & \underline{0} \\ \underline{0} & \underline{K} \end{bmatrix}\begin{bmatrix} \underline{\phi} \\ \underline{d} \end{bmatrix} = \begin{bmatrix} \underline{u} \\ \underline{F} \end{bmatrix} + \begin{bmatrix} \underline{\varphi}_{ati} \\ \underline{\varphi}_{vib} \end{bmatrix}. \tag{17}$$

3. ARC for Dumbbell-Shaped Spacecraft

The proposed adaptive attitude controller is provided, and the stability of the closed-loop system is proved. According to the first equation of Equation (16), the state equation of the dumbbell-shaped spacecraft system is as follows:

$$\frac{dx_1}{dt} = x_2, \tag{18}$$

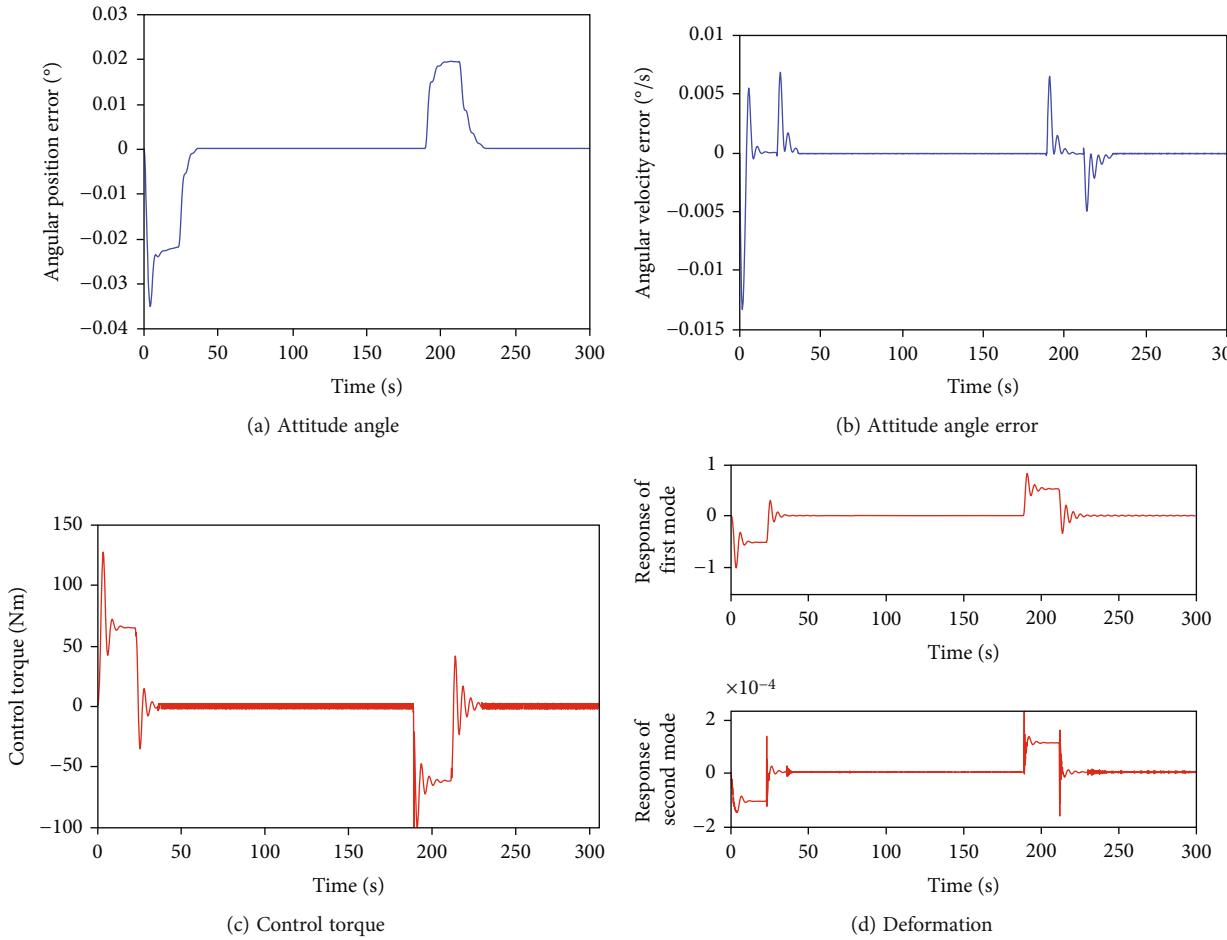

(a) Attitude angle

(b) Attitude angle error

(c) Control torque

(d) Deformation

FIGURE 14: Simulation results of ARC control: (a) angular position error of ARC control, (b) angular velocity error of ARC control, (c) control torque profile of ARC control, and (d) response of the first two modes.

$$J\frac{dx_2}{dt} = u + \Delta, \tag{19}$$

$$y = x_1. \tag{20}$$

$\boldsymbol{x} = [\phi \quad \dot{\phi}]^T$ is the attitude angle and attitude angular velocity of dumbbell-shaped spacecraft, J is unknown moment of inertia of dumbbell-shaped spacecraft system, and Δ represent the total uncertain nonlinear term including nonlinear term, external disturbance, cross-influence term, and uncertain part of model. u is the control input, and y is the attitude, angle, and position output of the dumbbell-shaped spacecraft.

The dumbbell-shaped spacecraft state space (Equation (19)) can be rewritten as follows:

$$J\frac{dx_2}{dt} = u + \Delta_n + \tilde{\Delta}, \tag{21}$$

where Δ_n is the nominal value of the total disturbance Δ and $\tilde{\Delta} = \Delta - \Delta_n$. In order to reduce the influence of parameter uncertainty and improve steady-state performance, online parameter adaptation is needed. Define $\theta = [J \quad \Delta_n]^T$. Equation (21) can be linearized according to unknown parameters and expressed as follows:

$$\theta_1\frac{dx_2}{dt} = u + \theta_2 + \tilde{\Delta}. \tag{22}$$

Make the following reasonable assumptions:

Assumption 1. The degree θ of parameter uncertainty and uncertainty nonlinearity is known:

$$\boldsymbol{\theta} \in \Omega_\theta \triangleq \{\boldsymbol{\theta} : 0 < \boldsymbol{\theta}_{\min} \le \boldsymbol{\theta} \le \boldsymbol{\theta}_{\max}\}, \tag{23}$$

where $\theta_{\min} = [\theta_{1\,\min}, \theta_{2\,\min}]^T$ and $\theta_{\max} = [\theta_{1\,\max}, \theta_{2\,\max}]^T$ are known. The $<$ symbol indicates that the corresponding elements of two vectors perform operations.

Assumption 2. The uncertain nonlinear term $\tilde{\Delta}$ is bounded and expressed as

$$\tilde{\Delta} \in \Omega_{\tilde{\Delta}} = \left\{\tilde{\Delta} : \left|\tilde{\Delta}\right| \le \delta\right\}. \tag{24}$$

Note 1. Unknown concentrated interference is bounded. The magnitude and rate of vibration of flexible appendages

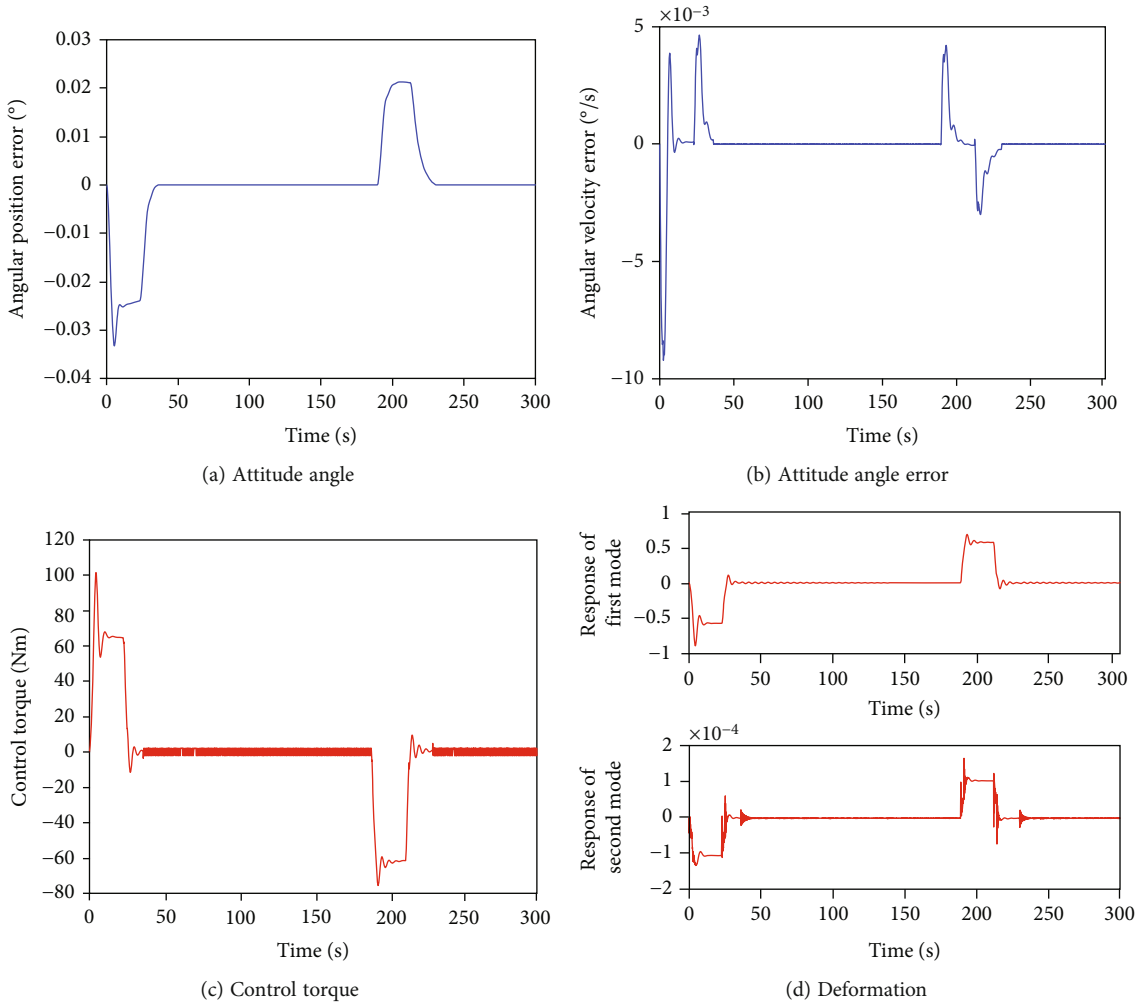

Figure 15: Simulation results of ARC+CSVS-SPP control: (a) angular position error of ARC+CSVS-SPP control, (b) angular velocity error of ARC+CSVS-SPP control, (c) control torque profile of ARC+CSVS-SPP control, and (d) response of the first two modes.

Table 4: Performance indices of the four control strategies.

Control strategy	PD	DRC	ARC	ARC+CSVS-SPP
$t_s(s)$	306	215	213	217
$e_m(^\circ)$	2.42×10^{-1}	2.3×10^{-2}	3.7×10^{-2}	2.12×10^{-2}
$p_m(^\circ)$	1.42×10^{-3}	1.82×10^{-5}	2.56×10^{-7}	1.10×10^{-7}
$p_s(^\circ/s)$	3.45×10^{-4}	5.79×10^{-6}	5.05×10^{-6}	2.25×10^{-6}

are bounded, and the energy of multiorder modes in dynamic equations is finite. In addition, in practice, uncertain boundaries can usually be measured or estimated. Therefore, this assumption is reasonable.

Set $x_d(t)$ be the desired attitude angle trajectory of spacecraft. Assuming that it is known and bounded by the second bounded derivative, the control objective is to synthesize bounded control input u so that the actual position x_1 is as close $x_d(t)$ as possible despite various model uncertainties.

Define the synovial function as

$$s = \dot{e} + ce = x_2 - q, q \triangleq \dot{x}_d - ce, \tag{25}$$

where $e = \phi - \phi_d$ is the attitude angle tracking error of dumbbell-shaped spacecraft and c is a given positive constant. Solving the tracking problem of x_d is equivalent to making s as small as possible. Adaptive control rate u is composed of adaptive compensation term u_a, feedback term u_{s1}, and robust term. The ARC schematic diagram is shown in Figure 3, and the following control law is designed as

$$u = u_a + u_{s1} + u_{s2}, \tag{26}$$

$$u_a = \widehat{\theta}\dot{q}, \tag{27}$$

$$u_{s1} = -k_s s, \tag{28}$$

$$u_{s2} = -\eta \text{ sign } (s), \tag{29}$$

where k_s represents the positive feedback gain, $k_s > 0, \eta > D$. After taking the time derivative of s, replace $\dot{s}$ and u with

Equations (22) and (25), respectively, and get

$$\theta \frac{dx_2}{dt} = \widehat{\theta}\dot{q} - k_s s - \eta \operatorname{sign}(s) + \Delta, \tag{30}$$

where $\widetilde{\theta} = \widehat{\theta} - \theta$ is parameter estimation error and $\widehat{\theta}$ represents the estimated value of θ. Selection of adaptive control law:

$$\dot{\widehat{\theta}} = -\gamma \dot{q} s. \tag{31}$$

$\gamma > 0$ is the adaptive control law matrix.

The Lyapunov function is defined as

$$V = \frac{1}{2}\theta s^2 + \frac{1}{2\gamma}\widetilde{\theta}^2. \tag{32}$$

Equations (20), (23), and (28) are taken into Equation (30) and derived to obtain

$$\begin{aligned} \dot{V} &= \theta s\dot{s} + \frac{1}{\gamma}\widetilde{\theta}\dot{\widetilde{\theta}} = s[\theta(\dot{x}_2 - \ddot{x}_d + c\dot{e})] + \frac{1}{\gamma}\widetilde{\theta}\dot{\widehat{\theta}} \\ &= s[u + \Delta - \theta(\ddot{x}_d - c\dot{e})] + \frac{1}{\gamma}\widetilde{\theta}\dot{\widehat{\theta}} = s\left[\widetilde{\theta}(\ddot{x}_d - c\dot{e}) - k_s s - \eta sign(s) + \Delta\right] + \frac{1}{\gamma}\widetilde{\theta}\dot{\widehat{\theta}} \\ &= -k_s s^2 - |s|\eta + s\Delta + \widetilde{\theta}\left[s(\ddot{x}_d - c\dot{e}) + \frac{1}{\gamma}\dot{\widehat{\theta}}\right]. \end{aligned} \tag{33}$$

Substituting the adaptive control law (29),

$$\dot{V} = -k_s s^2 - \eta|s| + s\Delta < -k_s s^2 \le 0. \tag{34}$$

Because if and only when $s = 0, \dot{V} = 0$. That is, when $\dot{V} \equiv 0$, $s \equiv 0$. According to the LaSalle invariance principle, the closed-loop system is asymptotically stable; that is, when $t \longrightarrow \infty$, $s \longrightarrow 0$. The rate of convergence of the system depends on k_s. Because $V \ge 0$ and $\dot{V} \le 0$, then when $t \longrightarrow \infty$, V is bounded. It can be proved that $\widehat{\theta}$is bounded, but there is no guarantee that $\widehat{\theta}$ is converged to θ. In order to prevent the control input signal $u(t)$ from being too large due to too large of $\widehat{\theta}$, it is necessary to make the change of $\widehat{\theta}$ within the range $[\theta_{\min} \quad \theta_{\max}]$ through the design of the adaptive control law. A discontinuous projection mapping adaptive algorithm can be used to modify the Equation (34).

3.1. Projection Mapping. An adaptive robust design based on discontinuous projection is constructed to solve the robust tracking control problem by exploiting physically plausible information, such as the bounds of parameter changes and internal friction states. The parameter estimated value $\widehat{\theta}$ is updated by a parameter adaptive control law having the following form:

$$\dot{\widehat{\boldsymbol{\theta}}} = \operatorname{Proj}_{\widehat{\theta}}(\boldsymbol{\Gamma\tau}), \tag{35}$$

where $\boldsymbol{\Gamma}$ represents the adaptation rate matrix and $\boldsymbol{\tau}$ is the adaptive function.

The projection mapping of Equation (35) is

$$\begin{aligned} \operatorname{Proj}_{\widehat{\theta}}(\cdot) &= \begin{cases} 0 & \text{if } \widehat{\theta} = \theta_{\max} \text{ and } \cdot > 0, \\ 0 & \text{if } \widehat{\theta} = \theta_{\min} \text{ and } \cdot < 0, \\ \cdot & \text{otherwise,} \end{cases} \\ P1\ \widehat{\boldsymbol{\theta}} &\in \bar{\Omega}_\theta = \left\{\widehat{\boldsymbol{\theta}} : \boldsymbol{\theta}_{\min} \le \widehat{\boldsymbol{\theta}} \le \boldsymbol{\theta}_{\max}\right\}, \forall t, \\ P2\ \widetilde{\theta}^T &\left[\boldsymbol{\Gamma}^{-1}\operatorname{Proj}_{\widehat{\theta}}(\boldsymbol{\Gamma\tau}) - \boldsymbol{\tau}\right] \le 0, \forall \boldsymbol{\tau}. \end{aligned} \tag{36}$$

When $\widehat{\theta}$ exceeded the maximum value, if there is a trend of continuing to increase, that is $\dot{\widehat{\theta}} > 0$, the value $\widehat{\theta}$ remains unchanged, that is, $\dot{\widehat{\theta}} = 0$; when $\widehat{\theta}$ exceeded the minimum value, if there is a tendency to continue to decrease, that is, $\dot{\widehat{\theta}} < 0$, the value $\widehat{\theta}$ remains unchanged, that is, $\dot{\widehat{\theta}} = 0$.

4. CSVS-SPP

Because the flexible beam of dumbbell-shaped spacecraft easily vibrates during large-angle attitude maneuver, attitude path planning for dumbbell-shaped spacecraft is carried out. Firstly, for large-angle attitude maneuver, the time-fuel optimal control strategy is adopted to plan the parameters of control torque (size, shape, action duration, action moment, etc.). If vibration suppression is not considered, the optimal solution of rest-to-rest is the switching function of bang-off-bang. The attitude maneuver program that can complete the specified angle is found first. Then, bang-off-bang is used to introduce the active vibration suppression method of force component synthesis, so that the maneuver process can reach the specified attitude angle without suppressing vibration.

4.1. Time-Fuel Optimal Control. When considering the time-fuel optimal maneuver, the cost function is as follows:

$$\Phi = \int \left(k_t + k_f u|f|\right) \mathrm{dt}, \tag{37}$$

where k_t is the time weight coefficient, k_f is the fuel weight coefficient, and u is the control ability, $u = T_m/J$. J is the moment of inertia value, and f is the step function. According to the optimization theory, the time-fuel optimal solution of the rest-to-rest motion of the system is in bang-off-bang form as shown in Figure 4, and this instruction can be expressed as

$$\begin{bmatrix} A_i \\ t_i \end{bmatrix} = \begin{bmatrix} T_m & 0 & -T_m & 0 \\ 0 & \tau & t_2 & \tau + t_2 \end{bmatrix} \tag{38}$$

where A_i is the torque amplitude, but t_i is the moment when the torque changes, and T_m is the maximum control torque. The duration of control torque τ and the occurrence time t_2 of deceleration command are determined by time

weight coefficient, fuel weight coefficient, and maneuver angle θ_f.

$$\tau = \sqrt{\frac{k_t \theta_f}{u\left(k_t + 2uk_f\right)}}, t_2 = \frac{\theta_f}{u\tau}. \quad (39)$$

4.2. CSVS Design Principles. First, consider the undamped vibration system as follows:

$$\ddot{x} + \omega^2 x = f(t). \quad (40)$$

4.2.1. CSVS Theorem 1. For an undamped second-order system with zero initial condition (Equation (40)), if the vibration period is divided into n equal parts and the same component force is applied at the starting point of each equal part or at the period difference of integer times from the starting point, the system will move without vibration after all the forces are finished.

4.2.2. CSVS Theorem 2. For an undamped second-order system with zero initial condition (Equation (40)), if the m vibration periods p of the system are equally divided (m and p coprime) and the same component force is applied at the starting point of each equal division or an integer multiple period difference from the starting point, the system will move without vibration when all the forces are finished.

Prove as follows:

The special solution response to step force $f(t) = \begin{cases} 0, t < 0 \\ a, t \geq 0 \end{cases}$ is

$$x(t) = \frac{a}{\omega}\int_0^t \sin\left[\omega(t-\xi)\right]d\xi = \frac{a}{\omega^2}(1 - \cos \omega t). \quad (41)$$

Figure 5 shows the superposition response of two equal amplitude step forces; a is the step amplitude, applied at $t = 0$ and $t = T/2$. The responses of the two-step forces are cosine curves (Equation (41)). The response of the second step force cancels out the response of the first force, so that the response of the whole force is constant $2a/\omega^2$ after half period.

4.3. Component Synthesis Vibration Suppression Method-Seven-Section Path Planning (CSVS-SPP). Based on CSVS method, the set attitude maneuver force is shown in Figure 6, and the time history of angular velocity is shown in Figure 7. The 7 sections are accelerated A1, accelerated A2, accelerated A3, uniform B, decelerated C1, decelerated C2, and decelerated C3. This method is called component synthesis vibration suppression method-seven-section path planning (CSVS-SPP). The angular acceleration of the acceleration section is 3 normal numbers, of which $a_{A_2} = 2a_{A_1} = 2a_{A_3}$. The angular acceleration of deceleration section is three constants opposite to that of acceleration section, and $a_{C_2} = 2a_{C_1} = 2a_{C_3}$, and $a_{A_2} = -a_{C_2}$; the angular acceleration in the uniform velocity section B is zero.

5. Simulation and Analysis

First, the key technical parameters of dumbbell-shaped spacecraft are provided with reference [6], and the parameters are shown in Table 1. Section 5.1 verifies the correctness of the dumbbell-shaped spacecraft dynamic model. In Section 5.2, the simulation results of the desired attitude tracking response control are provided, and the simulation results of PD, DRC, and ARC are analyzed.

5.1. Model Validation. The natural frequencies and modes calculated by the dynamic modeling method are compared with ANSYS software, and the effectiveness of the dumbbell-shaped spacecraft dynamic model is verified. In the dynamic simulation, the first six bending modes are considered, and their formations are shown in Figure 8, and their natural frequencies are shown in Table 2.

Through the comparative analysis of the formation and the first six orders of ANSYS, it can be seen that the formation trend is consistent. The active module and nuclear reactor are included in this paper. Table 1 shows that the frequency calculation is accurate. The correctness of the dynamic model in this paper is fully proved.

5.2. Designed Attitude Angle Position. The flexible spacecraft is intended to perform 90° large-angle attitude maneuver. From the initial state of 0° to the desired attitude angle of 90°, both the initial and desired attitude angular velocities are 0°/s. According to the first-order frequency $\omega_1 = 0.2230Hz$, the calculated period is $T_1 = 4.4846s$, the BCB time planning parameters are $\tau = 22.9211s$ and $t_2 = 189.0761s$, and the CSVS-SPP time planning parameters are shown in Table 3.

The bang-off-bang and the CSVS-SPP planning angular position are shown in Figure 9.

The desired attitude angle of bang-off-bang is divided into three sections: acceleration section A, uniform section B, and deceleration section C. The desired attitude angle of CSVS-SPP is divided into seven sections; the acceleration is A1, A2, and A3; the uniform velocity section B; and the deceleration sections are C1, C2, and C3.The desired angular velocities for both methods are shown in Figure 10.

The control of the bang-off-bang is shown in Figure 11(a), and the control of the CSVS-SPP is shown in Figure 11(b). Comparing the vibration of the two methods, it can be seen that the energy and time of CSVS-SPP are the same as those of bang-off-bang, but the amplitude of vibration is obviously reduced, which is of great significance to the attitude accuracy and stability of spacecraft.

5.3. Simulation Results. Comparative analysis of four control strategies:

(1) PD+BCB: PD control law is $u = -k_p e - k_d \dot{e}$, control gain selection $k_p = 500, k_d = 220$

(2) DRC+BCB: the DRC control rate is Equation (24); the parameters are $c = 30$, $k_s = 80$, and $\eta = 2.01$. The initial parameter estimation is $\widehat{\theta} = [\mathrm{J} \quad 0]$; the interference term is $\Delta = 0.5 \operatorname{sign}(t)$, $\gamma = 300$

(3) ARC+BCB: other parameters are the same as the above parameters, among which $\theta_{\min} = [0.8\mathrm{J} \quad -0.1]$, $\theta_{\max} = [1.2\mathrm{J} \quad 0.1]$

(4) ARC+CSVS-SPP: other parameters are the same as the above parameters, in which the target path parameters of the trajectory are $T_u = 4.4846s$, $\tau = 22.9211s$, $t_2 = 189.0761s$, and $a_c = 0.01^\circ/s^2$

To measure the quality of each control strategy, the following performance metrics will be considered: (1) settling time t_s, the time and measured velocity it takes for the single-axis attitude angular position and velocity errors to converge to 1×10^{-2}°and 1×10^{-2}°/s; (2) peak error e_m, the maximum absolute value of the single-axis attitude angle position error to evaluate the transient performance; (3) aiming accuracy p_m refers to the root mean square value of the single-axis attitude angle position error between 250 and 300 s, as the final measure metrics to track performance; and (4) degree of stability p_s. The root mean square value of the single-axis attitude angular velocity error of 100~200 s is used to measure the steady-state performance.

The simulation results of PD-controlled large-angle attitude maneuver are shown in Figure 12. It can be seen from Figures 12(a) and 12(b) that the PD controller needs to execute 306 s to make the attitude angular position and attitude angular velocity error of the dumbbell-shaped spacecraft less than the set $1 \times 10 - 2^\circ$ and $1 \times 10 - 2^\circ$/s. It is obvious that the attitude angular position of the dumbbell-shaped spacecraft has a stable steady-state error. Figure 12(c) is the control torque curve. It is evident from Figure 12(d) that the higher-order vibrations of the modes are not excited.

Figure 13 is the simulation result of DRC. It can be seen from Figures 13(a) and 13(b) that the DRC controller needs to execute 215 s to control the attitude angular position and attitude angular velocity errors of the dumbbell-shaped spacecraft within the required range, and the attitude angular position has a small static steady-state error. Compared with the PD control, the steady-state time t_s is much smaller than the PD controller. The peak error is an order of magnitude smaller. The aiming accuracy p_m and degree of stability p_s are, respectively, two orders of magnitude smaller than those of the PD controller. The overall performance index is better than the PD controller. From the perspective of vibration, the vibration values of PD control and DRC control are larger.

For the simulation analysis of ARC control, when using ARC to control the large-angle attitude maneuver of the dumbbell-shaped spacecraft, the angular position and velocity errors are shown in Figures 14(a) and 14(b). It can be seen that ARC has higher control precision than DRC and PD control. However, there is no significant steady-state error in the angular position because of ARC adjustable model compensation. Steady-state error and residual vibration suppression are required. Therefore, the ARC+CSVS-SPP is adopted below to improve ARC.

Finally, the combined method of ARC+CSVS-SPP is used to realize the large-angle attitude maneuver and active vibration suppression of the dumbbell-shaped spacecraft. The simulation results are shown in Figure 15. It can be seen from Figures 15(a) and 15(b) that the time required to achieve the control accuracy is 217 s, which is similar to DRC and ARC, and the peak error e_m is smaller than the other three controllers. Aiming accuracy and degree of stability are also significantly better than ARC. The specific parameters are shown in Table 4. Therefore, the following conclusions can be drawn: the controller constructed by the ARC+CSVS-SPP can meet the requirements of large-angle attitude maneuvers for dumbbell-shaped spacecraft.

The simulation results of the above performance indicators are shown in Table 4. From the perspective of the performance index steady-state time t_s, the PD controller does not perform well in terms of fast response. The other three control strategies are similar, but significantly better than the PD controller. For the performance index peak error e_m, DRC, ARC, and ARC+CSVS-SPP are all reduced by an order of magnitude compared with PD control. In addition, compared with PD control and DRC control, the aiming accuracy p_m of ARC and ARC+CSVS-SPP is improved by 4 orders of magnitude and 2 orders of magnitude, respectively. In conclusion, the proposed ARC+CSVS-SPP control strategy has good results in transient performance, final tracking performance, and steady-state performance.

6. Conclusion

Aiming at the large-angle and fast attitude maneuver of dumbbell-shaped spacecraft, an active vibration suppression technology based on ARC and CSVS-SPP is proposed. The desired angular position of the spacecraft is planned by the proposed CSVS-SPP, and the attitude angular position is divided into seven sections. Compared with the traditional BCB method, the vibration of the aircraft can be effectively suppressed. The ARC attitude controller can simultaneously consider the uncertainty of the rotational inertia of the flexible spacecraft and externally induced disturbances. The ARC+CSVS-SPP controller guarantees the specified transient performance as well as steady-state performance. The simulation results show that in the presence of external disturbance and parameter uncertainty, the attitude maneuvering and vibration suppression of ARC+CSVS-SPP are better than PD control and DRC control.

Data Availability

The raw/processed data required to reproduce these findings cannot be shared at this time due to technical or time limitations.

Conflicts of Interest

The authors declare that they have no conflicts of interest.

References

[1] A. S. Koroteev, Y. A. Oshev, S. A. Popov et al., "Nuclear power propulsion system for spacecraft," *Thermal Engineering*, vol. 62, no. 13, pp. 971–980, 2015.

[2] J. Zhang, S. Lu, and L. Zhao, "Modeling and disturbance suppression for spacecraft solar array systems subject to drive

fluctuation," *Aerospace Science and Technology*, vol. 108, article 106398, 2021.

[3] Z. Ma, Z. Liu, H. Zou, and J. Liu, "Dynamic modeling and analysis of satellite detumbling using a brush type contactor based on flexible multibody dynamics," *Mechanism and Machine Theory*, vol. 170, article 104675, 2022.

[4] H. Zhang, H. Liu, and D. Li, "Study of dynamics simulation on large space deployable membrane structures," *Chinese Journal of Space Science*, vol. 38, no. 1, pp. 101–108, 2018.

[5] D. A. Litvinov, N. V. Nunes, A. I. Filetkin et al., "The antenna phase center motion effect in high accuracy spacecraft tracking experiments," *Advances in Space Research*, vol. 68, no. 10, pp. 4274–4291, 2021.

[6] B. Wang, Z. Liu, and P. Zheng, "Rigid-flexible coupling dynamic modeling and analysis of dumbbell-shaped spacecraft," *Aerospace Science and Technology*, vol. 126, p. 107641, 2022.

[7] E. I. Abouelmagd, J. L. G. Guirao, and J. A. Vera, "Dynamics of a dumbbell satellite under the zonal harmonic effect of an oblate body," *Communications in Nonlinear Science and Numerical Simulation*, vol. 20, no. 3, pp. 1057–1069, 2015.

[8] E. I. Abouelmagd, J. L. G. Guirao, A. Hobiny, and F. Alzahrani, "Stability of equilibria points for a dumbbell satellite when the central body is oblate spheroid," *Discrete and Continuous Dynamical Systems - Series S*, vol. 8, pp. 1047–1054, 2015.

[9] Z. Liang and F. Liao, "Periodic solutions for a dumbbell satellite equation," *Nonlinear Dynamics*, vol. 95, no. 3, pp. 2469–2476, 2019.

[10] K. Shi, C. Liu, Z. Sun, and X. Yue, "Coupled orbit-attitude dynamics and trajectory tracking control for spacecraft electromagnetic docking," *Applied Mathematical Modelling*, vol. 101, pp. 553–572, 2022.

[11] C. Liu, Z. Sun, D. Ye, and K. Shi, "Robust adaptive variable structure tracking control for spacecraft chaotic attitude motion," *IEEE Access*, vol. 6, pp. 3851–3857, 2018.

[12] G. Shan, L. You, X. Huifeng, and Y. ShuYue, "Dynamic sliding mode controller with variable structure for fast satellite attitude maneuver," *Mathematical Problems in Engineering*, vol. 2021, Article ID 5539717, 11 pages, 2021.

[13] C. Liu, X. Yue, J. Zhang, and K. Shi, "Active disturbance rejection control for delayed electromagnetic docking of spacecraft in elliptical orbits," *IEEE Transactions on Aerospace and Electronic Systems*, vol. 58, no. 3, pp. 2257–2268, 2022.

[14] M. N. Hasan, M. Haris, and S. Qin, "Vibration suppression and fault-tolerant attitude control for flexible spacecraft with actuator faults and malalignments," *Aerospace Science and Technology*, vol. 120, article 107290, 2022.

[15] S. Yang, J. Han, L. Xia, and Y. H. Chen, "An optimal fuzzy-theoretic setting of adaptive robust control design for a lower limb exoskeleton robot system," *Mechanical Systems and Signal Processing*, vol. 141, article 106706, 2020.

[16] H. Sun, Y.-H. Chen, and H. Zhao, "Adaptive robust control methodology for active roll control system with uncertainty," *Nonlinear Dynamics*, vol. 92, no. 2, pp. 359–371, 2018.

[17] S. Qinqin, W. Xiuye, and C. Ye-Hwa, "Adaptive robust control for dual avoidance–arrival performance for uncertain mechanical systems," *Nonlinear Dynamics*, vol. 94, no. 2, pp. 759–774, 2018.

[18] S. Roy and I. N. Kar, *Adaptive-Robust Control with Limited Knowledge on Systems Dynamics*, Springer, Singapore, 2020.

[19] Z. Yu, Y. Guo, L. Wang, and L. Wu, "Adaptive robust attitude control and active vibration suppression of flexible spacecraft," *Proceedings of the Institution of Mechanical Engineers Part G Journal of Aerospace Engineering*, vol. 231, no. 6, 2017.

[20] Z. Yu, Y. Guo, L. Wang, and L. Wu, "Adaptive robust attitude control and active vibration suppression of flexible spacecraft," *Proceedings of the Institution of Mechanical Engineers, Part G: Journal of Aerospace Engineering*, vol. 231, no. 6, pp. 1076–1087, 2017.

[21] C. Liu, X. Yue, K. Shi, and Z. Sun, "Inertia-free attitude stabilization for flexible spacecraft with active vibration suppression," *International Journal of Robust and Nonlinear Control*, vol. 29, no. 18, pp. 6311–6336, 2019.

[22] Y. S. Hamed, K. M. Albogamy, and M. Sayed, "Nonlinear vibrations control of a contact-mode AFM model via a time-delayed positive position feedback," *Alexandria Engineering Journal*, vol. 60, no. 1, pp. 963–977, 2021.

[23] T. Rybus, M. Wojtunik, and F. L. Basmadji, "Optimal collision-free path planning of a free-floating space robot using spline-based trajectories," *Acta Astronautica*, vol. 190, pp. 395–408, 2022.

[24] Y. Kim, W. Jung, and H. Bang, "Real-time path planning to dispatch a mobile sensor into an operational area," *Information Fusion*, vol. 45, pp. 27–37, 2019.

[25] Y. Hu, B. Wu, Y. Geng, and Y. Wu, "Smooth time-optimal attitude control of spacecraft," *Proceedings of the Institution of Mechanical Engineers, Part G: Journal of Aerospace Engineering*, vol. 233, no. 7, pp. 2331–2343, 2019.

[26] X. Zhang, X. Zhang, Z. Lu, and W. Liao, "Optimal path planning-based finite-time control for agile CubeSat attitude maneuver," *IEEE Access*, vol. 7, pp. 102186–102198, 2019.

[27] L. Zheng, Y. Guo, and A. Lai, "Path planning for large angle attitude maneuver of flexible spacecraft," *Journal of Huazhong University of Science and Technology*, vol. 39, pp. 232–234, 2011.